Fatigue crack propagation in a helicopter component subjected to impact damage

M. Fossati, M. Pagani, M. Giglio, A. Manes[*]

Politecnico di Milano, Dipartimento di Meccanica, via la Masa 1, Milano, Italy

ABSTRACT

Damage tolerant methodology is increasingly used in aeronautical components, especially due the fact that the Aviation Regulation requires such an assessment in case an accidental damage occurs. At present, there is a strong and actual interest in applying such procedures to helicopter components that are subjected to high frequency cyclic loads. In this paper, an investigation on a damaged transmission shaft for a tail rotor transmission of an actual helicopter has been carried out focusing on the fatigue crack propagation. A complete sequence of experimental tests was performed in order to create an actual ballistic damage and to subsequently check the damage tolerant behaviour. The shaft was damaged by oblique ballistic impact and was subsequently subjected to torsional fatigue loading. During the fatigue cycles several cracks propagated from the ballistic damages. Both of these steps (impact and fatigue loading) were also simulated by a complex modelling approach based on Finite Element Models and fracture mechanics theory. The comparison between the experimental and numerical results shows a good agreement but it underlines the need for a very refined modelling technique capable to replicate all the features associated with the damage in order to reliably simulate the subsequent propagation phase.
© 2020 The Authors. Production and hosting by Elsevier B.V. on behalf of China Ordnance Society. This is an open access article under the CC BY-NC-ND license (http://creativecommons.org/licenses/by-nc-nd/4.0/).

1. Introduction

Like several mechanical devices, helicopters components are subjected to combinations of high frequency cyclic loads. These loads can act in the presence of defects, which may have been introduced during the manufacturing process or generated during the operations. Such defects can therefore generate fatigue crack growth under multi-axial conditions and, considering the peculiarity of the helicopter system (high vibration level), even small defects can propagate to failure in a short period of time [1]. Damage tolerance principle is the principal design philosophy in aeronautics [2] as also specifically stated in the FAR 29.571, "Fatigue Tolerance evaluation of Metallic structures" [3]. At present, there is a strong and actual interest in applying damage-tolerance procedures to helicopter components, even for the case of a small defect (flaw) [4]. This is especially true for the development of an accurate and effective code for the crack growth analysis under the action of typical helicopter spectra. The accurate prediction of crack advancement through a structure under fatigue-based loading has become a new challenge in the field of numerical simulation. An experimental approach to damage tolerance is often very complex both for the damage creation and for the subsequent step of the fatigue tests. A reliable and efficient methodology for predicting crack propagation is therefore of interest both from a theoretical and an industrial point of view. A round-robin programme has been carried out with interesting results [5,6] in order to benchmark the ability of the industry to predict fatigue crack growth life in a simulated complex helicopter component under rotorcraft spectrum loading (to support the use of the damage tolerance approach).

As a general framework, numerical simulations based on the Finite Element (FE) and fracture mechanics principles methods have been employed in order to develop a damage tolerance approach to be used for the design and assessment of components [7—9]. However, such a numerical methodology has several drawbacks. The simulation of fatigue crack propagation through a finite element mesh generally needs the modification of the mesh

topology. The use of remeshing techniques (manual or automatic) is therefore required to model accurately the crack propagation [7,8,10]. Other techniques are under investigation [11—16] but they are still in the development phase especially in case of their application to complex components. Other complications may arise especially if the initial defects, generated during a harsh operation, create a complex damage shape and residual stress fields surrounding the damage, which is the case of the present paper.

In this paper fatigue crack propagation was investigated in a helicopter transmission shaft subjected to ballistic impact damage. As described in details in the following section, ballistic impacts were carried out with an impact configuration of a 45° angle of obliquity thus a critical condition for the component. Impacted shafts were subsequently tested in a torsion test system and service spectrum loading has been applied. Cracks nucleate from the damage (specifically the damage under investigation is composed of two holes separated by a septum, Fig. 1) and propagate due to the application of service loads. Numerical models of impact were built and the results of these numerical analyses (the impacted shaft) were used as a "test bed" for the subsequent crack propagation analyses. Crack parameters (Stress Intensity Factors, SIF) were therefore obtained by models in different conditions of loads and crack length. Finally, the acquired SIF values were processed in the NASGRO propagation law [18] in order to obtain the propagation of the crack versus the number of cycles and to compare the results with the experimental tests. The details of the application are reported in the present paper and the results are discussed with focus on the effect of the residual stress field (due to impact) on the crack propagation. The definition, application and critical discussion of a reliable and efficient procedure for damage tolerant assessment of such a complex scenario is therefore the most valuable and original part of the paper.

It's important to state that, due to the fact that the research herein reported was developed on an actual component (thus designed and manufactured to be installed on a flying machine), it is not possible to share all the data and most of the results are presented in a normalised way.

2. Ballistic and fatigue experimental tests

Projectile impacts potentially play an important role in the design of modern aeronautic frames and defence and security systems especially when the flight envelope is a low altitude one, typical of a helicopter. It is therefore crucial to evaluate the damage of highly critical components after a ballistic impact and guarantee the survivability of the system, even in the worst condition. Regarding helicopters, the tail rotor power transmission shaft is one of the fundamental parts for ensuring flight. The shaft extends over the whole tail boom and is very exposed especially during hovering manoeuvres. Therefore, research to investigate the ballistic impact and the subsequent residual structural integrity of this component is clearly required and is the main aim of this paper.

Experimental programmes of ballistic impacts were carried out considering a critical condition for the component. Considering that the tail rotor power transmission shaft is mainly subjected to torsional load, a tangential hit with a 45° angle of obliquity, with respect to the shaft longitudinal axis, was considered as the most critical damage and an armour piercing 12.7 mm calibre bullet at ordnance velocity was chosen as a threat, see Figs. 1 and 2 for a graphical depiction of the angle. Specifically Fig. 1c) show the actual impact scenario of the shat on the test rig. Details of the experimental procedure are reported in Ref. [10] although the size of the shaft and the bullet are slightly different. Specifically, the type of the bullet is different: a 7.62 ball (soft core) was previously used in Ref. [10] whereas an armour piecing 12.7 calibre was herein investigated.

As far impact velocity is concerned, the higher actual velocity available for the 12.7 calibre bullet has been selected: average velocity of projectiles during the six tests was 903 m/s. In the present activity, six tubular specimens made of Al 6061-T6 (that reproduce a portion of the actual shaft component) were impacted and subsequently subjected to fatigue torsional test. The shaft is identical to an actual component with the exception of the two extremities where flanges were welded in order to allow correct griping both during the impact simulation and the fatigue tests. A simple depiction of the damage morphology obtained during the test is shown in Fig. 1. The ballistic tests produced a damage composed of two holes, an entry and an exit hole. The two holes on the shaft are visible in a graphical depiction, see Fig. 1b and are clearly identifiable in Fig. 1a. The bullet enters in the bottom right part of the portion of the shaft depicted and exits in upper left part. The two holes are separated by a zone that is called the septum (the portion of shaft between the entry and the exit hole, see Fig. 1a). Furthermore, all the possible cracks that can growth from the tips of the two holes, for simplicity reasons depicted as an ellipse are also visible in Fig. 1a.
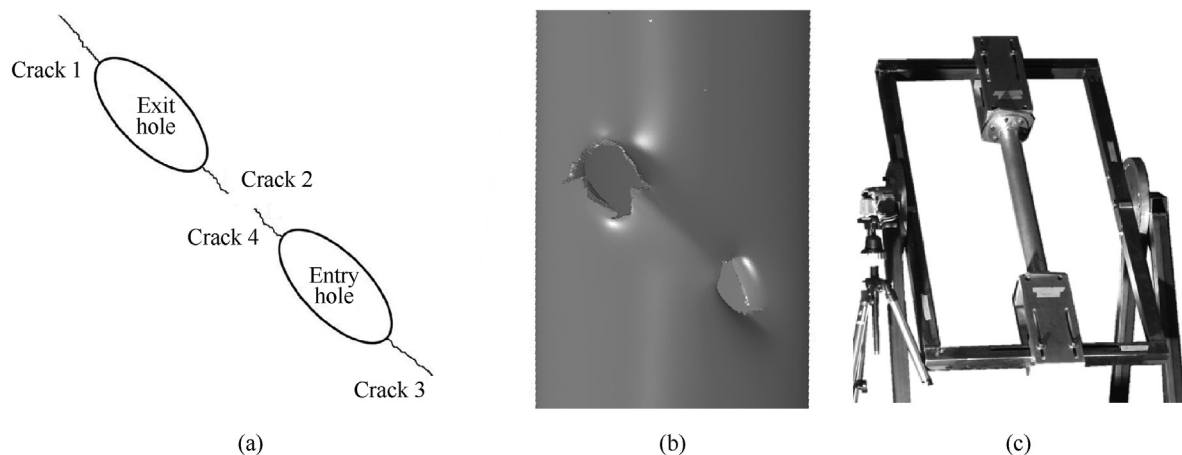

Fig. 1. a) Entry and exit hole depicted as an ellipse with the position and identification of 4 cracks (that propagate during the application of fatigue load)- b) virtual depiction of the damage due to ballistic impact Red axis refers to the relative position of measuring points of Fig. 5 -c) Actual impact scenario.
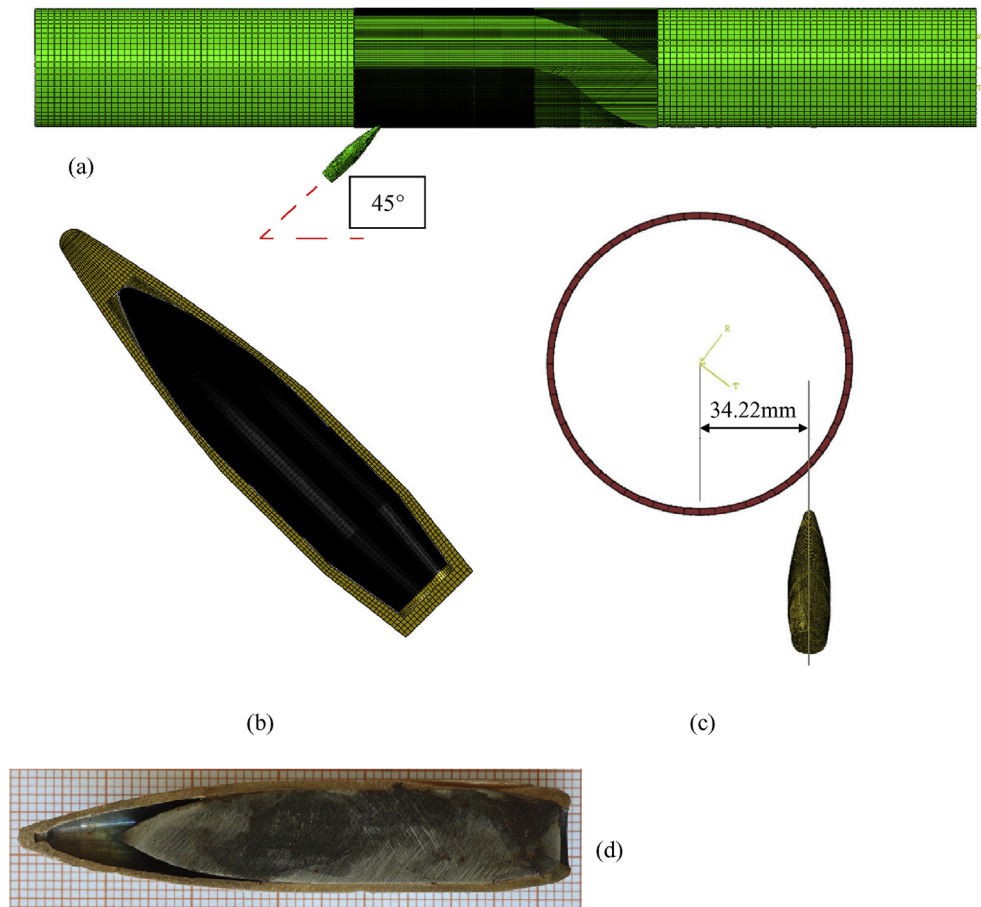
Fig. 2. Numerical models: a) two different mesh dimensions (near the impact zone and far from the impact zone) − b) numerical model of the projectile: deformable jacket and rigid core − c) numerical model of the shaft: the offset imposed to the bullet to replicate the experimental impact − d) picture of the actual bullet used for the creation of the numerical model.

A statistical analysis of the results obtained from the ballistic impact tests was carried out. The septum length was chosen as the major variable related to the variability of the impact phenomena. Variability in the impact condition of the bullet leads to a direct variability of the septum measurement. A probability plot of the septum measures was built using the normal distribution and the experimental data fit well a normal (Gaussian) distribution with a mean equal to 70 mm and a StDev equal to 14 mm. Also, the analysis of the damage morphology shows very similar results to the impact tests: the entry holes are almost elliptical (including the grazed area) while the exit holes have a more complex shape. More details about the size of the damage are reported in Section 3 when experimental data are compared with the results from the numerical models.

Subsequently fatigue torsional cycles were applied on damaged shaft specimens by means of a hydraulic multiaxial test machine MTS 809. Both a spectrum load replicating a flight mission and a constant amplitude fatigue load at different levels (on different damaged shafts) were applied. During the application of the load, fatigue cracks nucleate at the edge of the holes, and propagate from these points. Crack propagations was monitored by means of a Leica DFC290 optical microscope, equipped with the hardware and the software for image acquisition in order to measure the position of the crack with high precision in the early stage of propagation, and also by means of common optical measurement as soon as the crack length became relevant.

Experimental tests show that the primary crack propagation always starts from the exit hole along a path at a 45° angle and the propagating tip is oriented towards the external part of the ballistic damage, see crack 1 in Fig. 1. Subsequently crack 2 starts to propagate, initially also along a path at 45° angle, but then deviates in the proximity of the entry hole with a kink.

3. Numerical model characteristics

The numerical 3D simulations of the impact of 12.7 mm projectiles carried out using the finite element software Abaqus/Explicit for the simulation and the Abaqus CAE as a pre/post processor, as shown in Fig. 2. Fig. 2d) reports also a picture of a section of the actual bullet (with graph paper) in order to provide an insight in the size of the items. In the model, two different approaches were used during the modelling phase: the shaft and the jacket of the projectile were considered as deformable components and eight node brick elements (C3D8R) were adopted for the discretization. On the contrary, the core of the projectile was considered undeformable and was modelled with rigid shell elements (R3D4), Fig. 2b. This is justified by the fact that all the bullets used during the tests remain almost undeformed after the impact. Regarding the element dimensions, different refinements of the mesh were used: a dense and structured mesh was generated around the impact area while a coarser mesh was adopted elsewhere.

In Ref. [17] a similar case (numerical simulation of a ballistic impact on an aluminium tube) has been investigated and a mesh of

approximately of 0.5 mm size has been found effective in the simulation of such a type of failure. Due to the fact that the case of the present activity is similar but not equal, a dedicated sensitivity analysis has been performed starting from the findings of [17]. A suitable dimension for the contact zone elements was determined, achieving a good compromise between computational time and accuracy. The solution is convergent if the calculated residual velocity of the projectile differs less than 5% from the one calculated with a more refined mesh. The different element sizes tested are shown in Table 1: 4 elements discretization along the thickness was used (the configuration is described in the second row of Table 1). The final mesh is shown in Fig. 2a.

The model was constrained by a "perfect clamping" boundary condition, applied to the nodes positioned on the external free sections of the shaft, while the projectile was free to move; this constraint system exactly reproduces the one used during the ballistic damage introduction (i.e. the flange bolted to a very stiff picture frame constrained to the ground). A contact algorithm with an 'interior' option was activated between the shaft and the projectile. In the contact properties, no friction was considered.

3.1. Material models: constitutive relation and failure criteria

The use of a dedicated and reliable constitutive law of the involved materials (shaft and bullet) is very important in order to reproduce the plastic behaviour and failure. Temperature softening as well as hardening due to a high strain rate, element erosion and contact properties have to be considered in order to replicate experimental data both for macroscopical results (residual velocity of the bullet, type of the damage, extension of the damage) and for micromechanical features (residual stresses). The use of accurate results, obtained from the impact simulation model, is fundamental in the subsequent crack propagation analysis to develop a validated methodology for the assessment of damage tolerant prediction (i.e. crack propagation) in case of ballistic impact. The shafts used in the experimental tests are made of Al 6061-T6, an aluminium alloy containing silicon and magnesium as the main alloying elements. All the material parameters and a detailed description of the material behaviour are reported in Ref. [17].

As far as the failure criterion is concerned, the Bao-Wierzbicki (B—W) criterion was used [17]. The B—W's model is an evolution of the Johnson-Cook. It's a phenomenological criterion based on the accumulation of the plastic strain increments weighted by a function called fracture locus. The criterion has been obtained by empirical fitting of experimental data obtained by several failure tests carried out on specimens made of Al 6061-T6. All the details of the calibration including the parameters used in the present work are reported in Ref. [17]. Moreover in Ref. [17] also a validation failure test on a specimen cut directly from a tube is reported, in order to assess the transferability of the calibration data.

Considering the projectile materials, the 12.7 mm projectile was modelled in two detached parts, according to the experimental results, in which no deformation on the recovered core of the projectile and high deformation of the projectile jacket were observed. The steel core was therefore modelled as undeformable; whereas the CuZn30 brass sabot was modelled as deformable. A Johnson-Cook (JC) constitutive law was chosen to describe the CuZn30 brass behaviour of the sabot. This is expressed by Eq. (1).

$$\sigma = \left[A + B \cdot (\varepsilon_p)^n\right]\left[1 + C \cdot ln\left(\frac{\dot{\varepsilon_p}}{\dot{\varepsilon_0}}\right)\right]\left[1 - \left(\frac{T - T_a}{T_f - T_a}\right)^m\right] \quad (1)$$

where A is the elastic limit, B and n are the characteristic constants of the plastic behaviour, C expresses the sensitivity to the strain rate, $\dot{\varepsilon_0}$ is the reference strain rate (typically set to 1 s-1), ε_p and $\dot{\varepsilon_p}$ respectively the plastic strain and the plastic strain rate, T, T_a, T_f are respectively the actual temperature, room temperature (293 K) and the melting temperature in the absolute scale, m is a material constant for the temperature dependency.

In this case, the numerical law that ruled the failure of the brass sabot was the Johnson-Cook (JC) damage model, whose coefficients are available in the literature [20]. The model used is:

$$\varepsilon_f = \left[D_1 + D_2 exp\left(D_3 \cdot \frac{\sigma_H}{\sigma_{vm}}\right)\right] \cdot \left[1 + D_4 \cdot ln\frac{\dot{\varepsilon_p}}{\dot{\varepsilon_0}}\right] \cdot [1 + D_5 T] \quad (2)$$

in which, the coefficients from D1 to D5 are the material constants, whose numerical values are reported in Table 2, σ_h is the hydrostatic stress, σ_{vm} is the Von Mises equivalent stress, $\dot{\varepsilon_0}$ is the plastic strain rate, $\dot{\varepsilon_p}$ is a reference strain rate and T^* is the homologous temperature. All the coefficients of the JC models for the CuZn30 brass are reported in Table 2: These coefficients were obtained from the literature [20], but their reliability was previously verified by the same authors in another impact analyses [19].

3.2. Initial projectile position and velocity

The offset of the projectile (in the numerical analysis), the distance between the longitudinal axis of the shaft and the longitudinal axis of the bullet Fig. 2c, was chosen in order to reproduce the damage conditions as close as possible to the experimental ones, as specified in the next chapter, while the oblique angle, i.e. the angle between the direction (axis) of projectile and the longitudinal direction of the shaft, was set to 45°. The offset between the axis of the shaft and the axis of the projectile was set to 34.22 mm. Moreover, the initial velocity modulus was averaged over the data measured in the experimental tests: the initial velocity of projectile

Table 1
Dimension of the elements in the different analyses, each row is a configuration of mesh parameters used to verify mesh convergence.

Number of elements in the dense zone along the thickness	Dimension of the element in the dense zone /mm	Dimension of the element in the coarse zone /mm
3	0.6	0.95
4	0.475	0.95
5	0.38	0.95

Table 2
Constant for the JC constitutive laws model: Brass CuZn30 [20].

Constant	Numerical value
ρ /(kg·m^3)	8520
E/MPa	115000
ν	0.33
Cp /(J·kg^{-1}·K^{-1})	385
α (K^{-1})	1.99·10-5
$\dot{\varepsilon_0}$ (s^{-1})	1
A /MPa	111.69
B /MPa	504.69
C	0.009
n	0.42
m	1.68
T_m /K	1189
D_1	0.0
D_2	2.65
D_3	−0.620
D_4	0.028
D_5	0.0
ε_f	0.024

was 903 m/s. The impact tested shaft represents a section of the rear tail transmission of a helicopter hence, for the real working conditions, the impact between the shaft and the bullet should take the rotation of the shaft into consideration. The experimental reproduction of such condition is very complex indeed. It was however demonstrated for a similar configuration in Ref. [17], that the rotation of the shaft does not significantly influence the impact damage. The rotation velocity of the shaft (usually between 2000 and 3000 RPM) modifies the relative impact velocity by a small amount of about 10−20 m/s, thus a very reduced amount compared with impact velocity of 903 m/s. Therefore, all the procedure described in this paper do not consider the effect of the rotation of the shaft.

3.3. Simulation of the impact

This phase was aimed at obtaining a representative model of the damaged shaft, presenting two perforation holes generated by the numerical impact simulation. Subsequently the result of this model
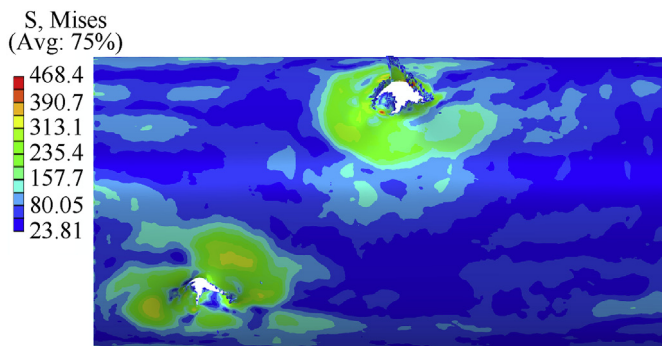

Fig. 3. Numerical simulation of the damage in the impact area.

was used for the next numerical analysis for the crack propagation prediction. Thus, the numerical model that reproduces the impact test phase is very important for the reliability of the damage propagation analysis: this model has to reproduce in a very refined and realistic way all the damage features, including petalling and residual stresses. This requirement is fundamental for a reliable numerical model capable of replicating the state of stress at the tip of the propagating cracks. As explained above, in the numerical analyses a specific offset was chosen to generate damage in the shaft as close as possible to the experimentally obtained one, see Fig. 2c. Due to the variability of the damage obtained in the experimental tests, a target damage shape (an experimental average one) was chosen to validate the numerical results. Considering Figs. 3 and 4, the numerical simulation can clearly reproduce not only the dimension of the hole but also the shape features (basically petalling), generated by the impact of the 12.7 mm projectile. Entry and exit hole can in fact be considered as elliptical with a major axis, 2a, aligned to the bullet direction and a minor axis, 2b perpendicular to the bullet direction. The experimental holes show an average value for the entry holes of $2a = 18$ mm, $2b = 13$ mm whereas from the numerical model $2a = 22$ mm and $2b = 16$ mm. For the exit holes the experimental average values are $2a = 23$ mm and $2b = 14$ mm whereas from the numerical model the values are $2a = 23$ mm and $2b = 16$ mm. As far as the septum is concerned, the experimental average value is 73 mm whereas the numerical average from the model is 72 mm. Finally, also for the exit velocity the comparison shows a good match: 870 m/s is the average exit velocity acquired during the experimental tests that can be compared with the numerical value of 886 m/s. Moreover, the numerical simulation shows that only 4% of the initial energy is absorbed during the impact.

The damage geometry data and the velocity results demonstrate a very small difference between the numerical data and the experimental results, thus highlighting the capability of the numerical model to correctly predict the damage inside the shaft.
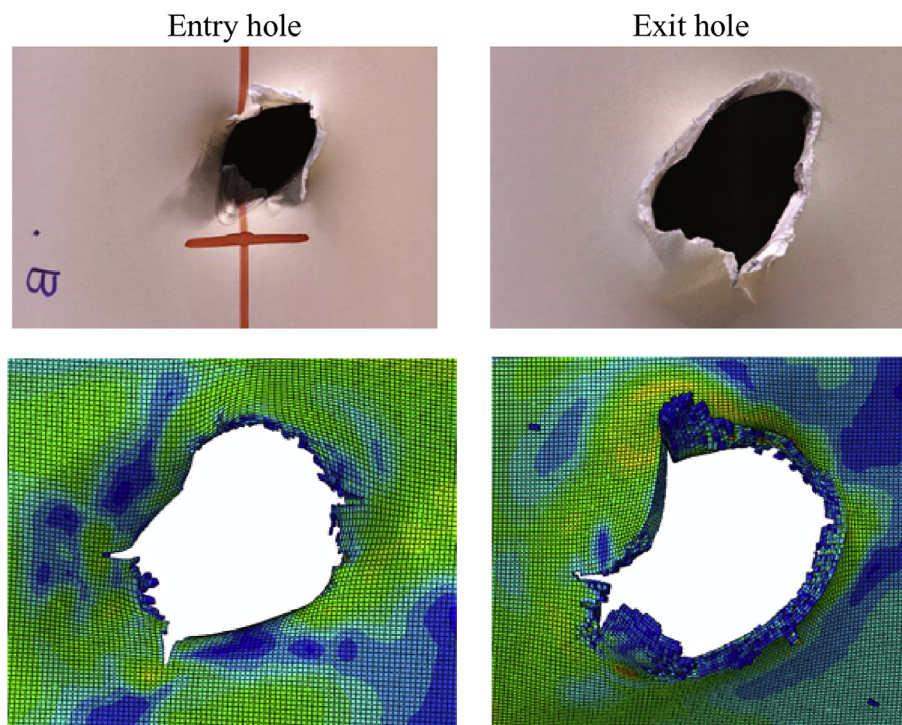

Fig. 4. Experimental and Numerical entry and exit holes.

(a) Comparison of residual axial stress

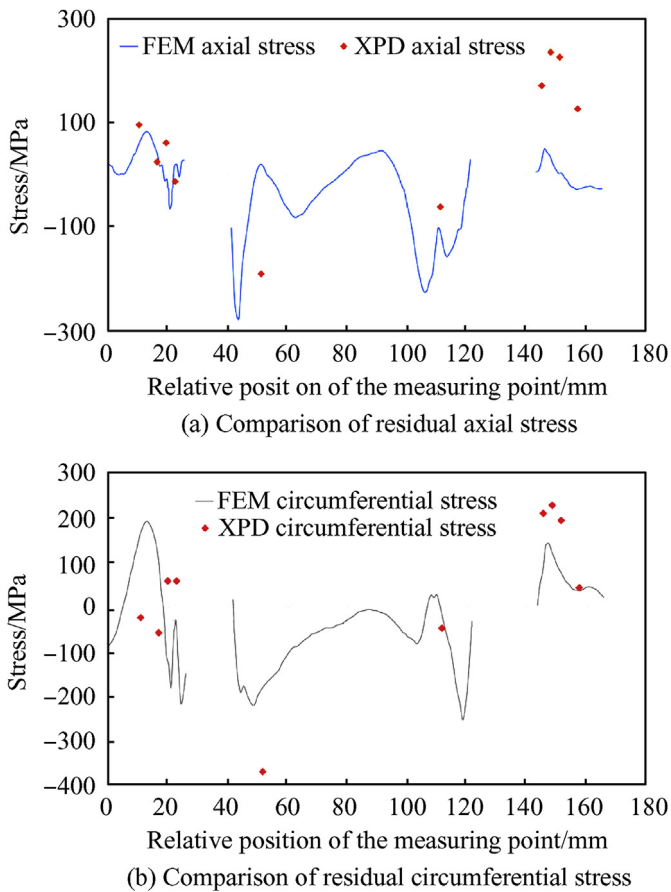(b) Comparison of residual circumferential stress

Fig. 5. Comparison between experimental (XRD) and Numerical (FEM) residual stress in a cylindrical reference frame a)axial, b)circumferential.

Another important comparison was carried out on the local stress patterns. The surface residual stresses of the impacted shaft were measured using an X-ray voltage analyser Stresstech Group V.1.01. A 2-mm collimator dimension was used with 60 s exposure time, 11 measurements for each angle and 3 angles (0°,45°,90°) for each point. On each shaft measurements were performed in 10 points along a straight line inclined at 45° degrees: 4 points outside of each hole respectively at about 3, 6, 9 and 15 mm from the hole border and 2 internal points (along the septum) approximately at 10 mm from the nearest hole's border. Residual Stresses were converted in a cylindrical reference frame and values in axial and circumferential direction were compared with the values obtained from the numerical analyses. Experimental average stress values and the numerical stress trend (both in axial and circumferential direction) are depicted in Fig. 5 showing good agreement.

The relative position in Fig. 5 refers to a straight line starting from the exit hole zone towards the entry hole zone, thus two parts of the graph do not show any data due to are the area of the holes. In Fig. 1 a red axis is reported. It refers to the X axes of Fig. 5. It is shifted upward for sake of clarity but it is supposed to be aligned with the tips of the damages.

Reliable impact simulation in terms of damage geometry and residual stress field is a key feature as these parameters are the main input data for the subsequent crack propagation analysis.

4. Simulation of crack propagation

As shown above the fatigue experimental tests showed the

nucleation and propagation of cracks from holes generated by the impact of the projectile. The nucleation and propagation phenomenon was subsequently simulated by means of numerical models. Firstly, the numerical model of the impacted shaft was used to exploit a dedicated approach for the calculation of the Stress Intensity Factors, SIF (K factors, K_I, K_{II}, and K_{III}), that allows the description of the state of stress of the tip of the cracks at different values of load and crack length. The fracture parameters and the SIF, were subsequently exploited using the NASGRO equation [18] to calculate the crack growth rate and to be compared with the experimental data. SIF parameters were evaluated at different loading levels (discussed in this section below) with two sets of analyses: with and without the residual stresses pattern (due to impact) in order to verify their influence. It's important to remark that the results of the numerical analyses of the impact (the impacted shaft) were used as a "test bed" for the subsequent crack propagation analyses. However, two models were considered: one complete model with deformed shape and residual stresses due to the ballistic impact and a second model only with the deformed shape (without residual stresses on the mesh). Especially in the first part of the propagation, the crack tip is strongly influenced by the surrounding stress pattern. These simulations permit the investigation of the effect of this feature on the residual resistance of the shaft thus being as close as possible to the real condition of the stress present in the shaft after the impact of the projectile.

Focusing on the simulations to calculate the K parameters, a crack path was reproduced in the exit hole, see Fig. 6a. The elements along the crack propagation paths were cut diagonally forming couples of wedge elements (45° angled with respect to the axis of the tube). 45° degree angles were chosen due to the fact that experimental assessments showed that cracks follow this direction. This is the only assumption made in the modelling method and it's functional at the building of a predictive tool (the MATLAB routine exploiting NASGRO equation) for crack propagation assessment. In each analysis, a set of appropriate coupling constraints was introduced between the two faces of the cracks in order to obtain the desired length with a limited numerical effort. Prior to the simulation of the crack propagation, a verification of the most critical
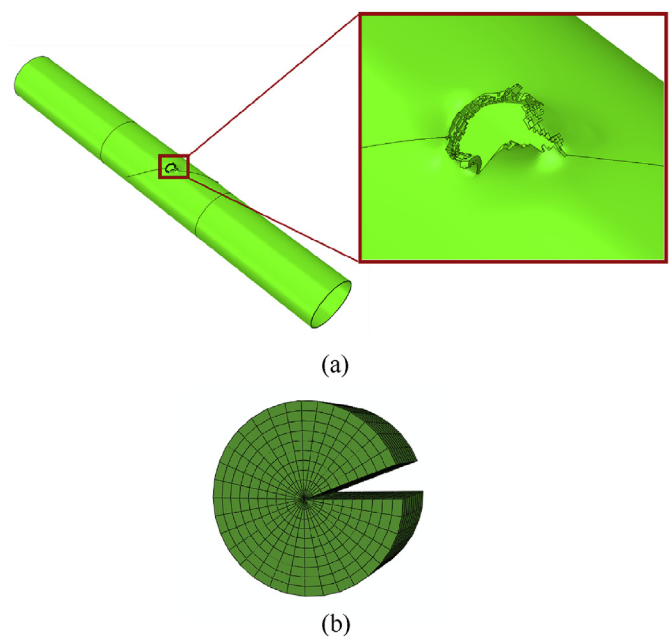

(a)

(b)

Fig. 6. a) The Crack in the FE model – b) Submodel used for the calculation of SIF values.

points from where a crack could have started was carried out. Small cracks were introduced around the entry and exit holes and the local SIFs were computed under the torsional load. The results were in good agreement with the experimental outcome: two opposite cracks around the exit hole were identified as the most critical for the propagation analysis. Analyses of the SIF values were performed for a discrete length of the crack starting form a very short crack to the maximum propagation obtained the during experimental tests (L_{max}). Different combinations of cracks ($L_{1\#}$-$L_{2\#}$) were therefore considered for the evaluation of the K factors close to the exit hole (see Fig. 6a where crack 1 and 2 of Fig. 1 are present). Crack lengths were set to $L_{1\#}$ for crack 1 and to $L_{2\#}$ for crack 2, see Fig. 1. The length of the cracks are considered starting from the hole. The configuration of the crack lengths considered during the analysis are reported below.

For crack 1 of Fig. 1, the external crack lengths (measured from the side of the hole) were: $L_{11} = 0.08 \cdot L_{max}$ - $L_{12} = 0.16 \cdot L_{max}$ - $L_{13} = 0.33 \cdot L_{max}$ - $L_{14} = 0.5 \cdot L_{max}$ - $L_{15} = L_{max}$.

For crack 2 of Fig. 1, the internal crack lengths were: $L_{21} = 0.04 \cdot L_{max}/L_{22} = 0.08 \cdot L_{max}/L_{23} = 0.33 \cdot L_{max}/L_{24} = 0.5 \cdot L_{max}$.

All the 20 combinations of cracks, see Table 3, were investigated. However due to the fact that residual stresses are present, the calculation of the crack parameters is not linear with respect to the loading condition thus also the loading condition requires a complex set up. As far as the constrains are considered, one side of the tube is fully constrained while only the axial displacement and the axial rotation are constrained on the other side (in order to reproduce the experimental constrains of the test system). The load was applied as a torque, directed as the axes of the specimen, in order to open the crack, thus in the worst condition (as for the experimental tests). According to experimental tests programme six loading conditions were identified in terms of Mean torque (CMed) and Amplitude Torque (Camp). These conditions include the zero-loading condition that is influenced only by the residual stress pattern. For each case of Table 3, a 6-step ramp, from zero torque to the maximum torque (Cmed + Camp), was used in the numerical simulations to account for the non-linear behaviour introduced by the residual stresses and the contact interaction between the two sides of the crack that was considered in all the simulations. This procedure was repeated for all the 6 configurations thereby providing a matrix of crack parameters data that can be used to simulate several crack propagations (under several loading conditions under the hypothesis of a linear method). Analyses were performed exploiting the models with and without residual stresses.

At the end of each calculation, a special sub-model (see Fig. 6b), assembled with focused mesh elements positioned around the tip of each crack, was used to acquire the SIF for each load case, exploiting Abaqus automatic calculation. Similar approach has been used by authors in Ref. [21]. Using the refined strain patterns obtained by the submodel, Abaqus calculates the SIF values in 11 different points along the thickness and an average value is calculated. The averaged SIF calculated for each crack are finally a function of the crack length and the torque ratio. All possible combinations between them were considered during the analyses. A complete map of K values was obtained by interpolating the results found with different load conditions and different crack lengths.

4.1. Crack growth model: Matlab Routine

After the evaluation of the K factors (K_I, K_{II}, and K_{III}) an appropriate MATLAB routine was compiled in order to obtain the curve crack length/number of cycles exploiting the NASGRO formulation [18].

NASGRO is a crack growth model for the estimation of the growth of fatigue cracks, under cycling loading. The fatigue crack grow rate (da/dN) is described by a series of parameters as a function of material, mechanical behaviour and the stress intensity factor range.

$$\frac{da}{dN} = C \cdot \left[\left(\frac{1-f}{1-R} \right) \cdot \Delta K \right]^n \cdot \frac{\left(1 - \frac{\Delta K_{th}}{\Delta K} \right)^p}{\left(1 - \frac{K_{max}}{K_c} \right)^q} \tag{3}$$

Herein a brief description of the parameters of equation (3), however more details about the NASGRO model were reported in Ref. [18]. Parameters that describe fracture behaviour of the material of the shaft (Al 6061-T6) were also obtained from the database in Ref. [18] (Table 5).

C crack growth constant
f crack opening function
ΔK stress intensity factor range
ΔK_{th} threshold of stress intensity factor range for crack propagation
K_c fracture toughness
K_{max} maximum stress intensity factor
n Paris exponent
p,q empirical constants describing the curvatures that occur near the threshold and near the instability region of the crack growth curve, respectively
R load ratio

Finally, a Matlab Routine was compiled to obtain the curve crack length/number of the cycles and the variation of the SIF during the crack growth. The routine receives as input the values of the SIFs at different crack lengths, at different loads, and the load story and calculates the crack growth. The threshold K of each crack is taken into account to verify if cracks fail to initiate propagating.

The Matlab routine calculates the propagation under a predefined number of cycles at a certain load level, defined as a mean and an alternate torque. The Matlab routine exploits a simple linear method that doesn't take the interaction effect between load cycles of different amplitude into account. The calculation is carried out until the achievement of the K_C.

As previously underlined, due to the fact that the research herein reported was developed on an actual component, it is not possible to share all the data and most of the results are presented in a normalised way. The number of Cycles (N_{cycle}), the length of the crack (c) and the stress intensity factor (ΔK_{eq}) are calculated by this procedure and presented in a normalised way as a ratio with the maximum values obtained during test 1 (N_{max}, C_{max}, ΔK_{eqmax}).

Several fatigue tests were carried out. One specimen was tested using a spectrum load that replicates a flight mission with severe loading condition. This experimental test shows no crack propagation and, at the same time, also the modelling approach shows a SIF value lower than the threshold values, thus no propagation was

Table 3
Combination of crack lengths (limited to crack 1 and crack 2) considered during the FE crack propagation.

	L_{21}	L_{22}	L_{23}	L_{24}
L_{11}	L_{11}_L_{21}	L_{11}_L_{22}	L_{11}_L_{23}	L_{11}_L_{24}
L_{12}	L_{12}_L_{21}	L_{12}_L_{22}	L_{12}_L_{23}	L_{12}_L_{24}
L_{13}	L_{13}_L_{21}	L_{13}_L_{22}	L_{13}_L_{23}	L_{13}_L_{24}
L_{14}	L_{14}_L_{21}	L_{14}_L_{22}	L_{14}_L_{23}	L_{14}_L_{24}
L_{15}	L_{15}_L_{21}	L_{15}_L_{22}	L_{15}_L_{23}	L_{15}_L_{24}

Table 4
Torque Ratio applied over the Load Step.

Step Case	Mean Torque	Amplitude Torque
C_1	CMed	$0.32 \cdot$ CAmp
C_2	CMed	$0.5 \cdot$ CAmp
C_3	CMed	$0.66 \cdot$ CAmp
C_4	CMed	$0.83 \cdot$ CAmp
C_5	CMed	CAmp

obtained. Additional five tests were carried out with a constant amplitude fatigue load and load levels were chosen in order to cause propagation. The five tests were performed at 5 different level, as shown in Table 4, of constant amplitude fatigue torsional load. The load varies from minimum level (level 1, C_1) to a more severe level (level 5, C_5) where only a few cycles were completed before failure. Fig. 7 reports the experimental data and the results obtained from the numerical modelling can therefore be compared, as mentioned above, in a normalised way: the actual cycles carried out in each test were therefore normalised with the number of cycles achieved during torque level C_1, the lowest level included in Table 4. It is worth stressing that the data reported in terms of number of cycles before failure are the number of cycles between the nucleation of the crack and the failure of the shaft, for both the experimental and the numerical simulation. In fact, a correct comparison with the experimental data needs to consider only the

Table 5
NASGRO crack growth parameters (Al 6061-T6) [18].

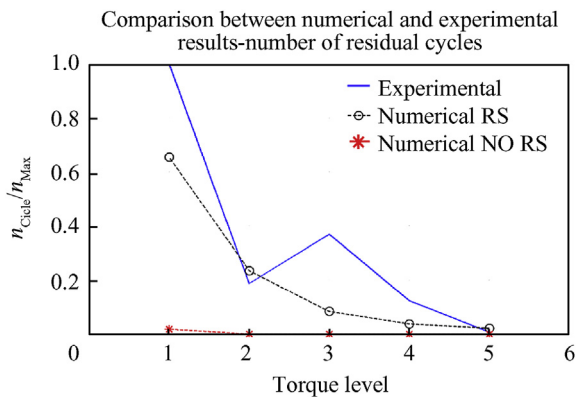| Parameter	Value
σ_{YS} /MPa	282.7
K_{Ie}/(MPa$\sqrt{\text{mm}}$)	1251
K_{Ic} /(MPa$\sqrt{\text{mm}}$)	938.2
UTS /MPa	310.3
A_k	1
B_k	0.75
a_0 /mm	0.0381
n	2.30
p	0.5
q	0.5
C	5.079 E$-$10
C_{th}^p	1.5
C_{th}^m	0.1
ΔK_I /(MPa$\sqrt{\text{mm}}$)	45.52
Std. α	2.0

Fig. 7. Results of the analyses. Number of residual cycles before failure vs torque level. Comparison between numerical and experimental results - with (RS) and without (NO RS) residual stresses.
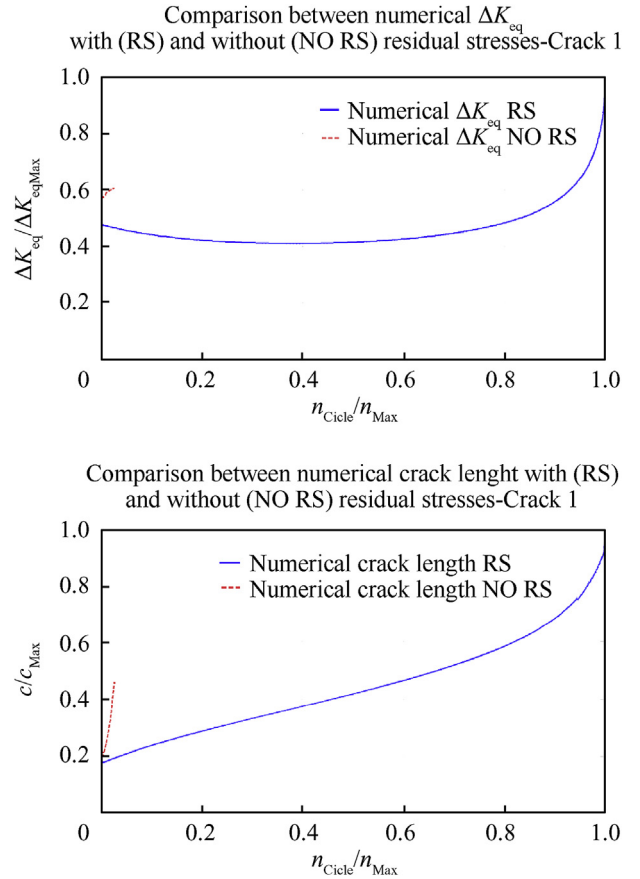

Fig. 8. Results of the analyses $C_{Max} = C_1 -$ Crack 1. Comparison between results obtained with (RS) and without (NO RS) residual stresses. ΔK_{eq} vs n_{cycle} and crack propagation (c is the length of the crack) vs n_{cycle}.

net cycles between the crack detection and the final failure.

The comparison graph shown in Fig. 7, reports both the results of the analyses with residual stress (black line $-$ Numerical RS) and without residual stress (red line $-$ Numerical NO RS). Only by including the residual stress in the analysis, an accurate evaluation of the residual life of the shaft after the impact can be obtained. Considering the results obtained without the residual stress, the analysis considerably underestimates the residual resistance of the shaft.

Fig. 8 (Crack 1) and Fig. 9 (Crack 2) report the results obtained with the numerical simulation of the crack propagation for C_1, see Table 4, in order to better investigate in the role of the RS. The end of the curves is defined by the achievement of the K_C. In particular, a comparison between the results obtained with and without the introduction of residual stresses (inside the numerical models from which K values have been calculated) is reported. The graphs clearly show how the introduction of residual stresses substantially alters the crack propagation. In fact, there is a sensible reduction in the value of ΔK_{eq} and therefore also a reduction in the crack growth rate. The presence of residual stress induces beneficial effects that drastically relax the state of stress at the tip of the propagating cracks thus delaying the achievement of the K_C.

5. Comparison between numerical and experimental approaches: stress state

During the crack growth experimental tests, three different
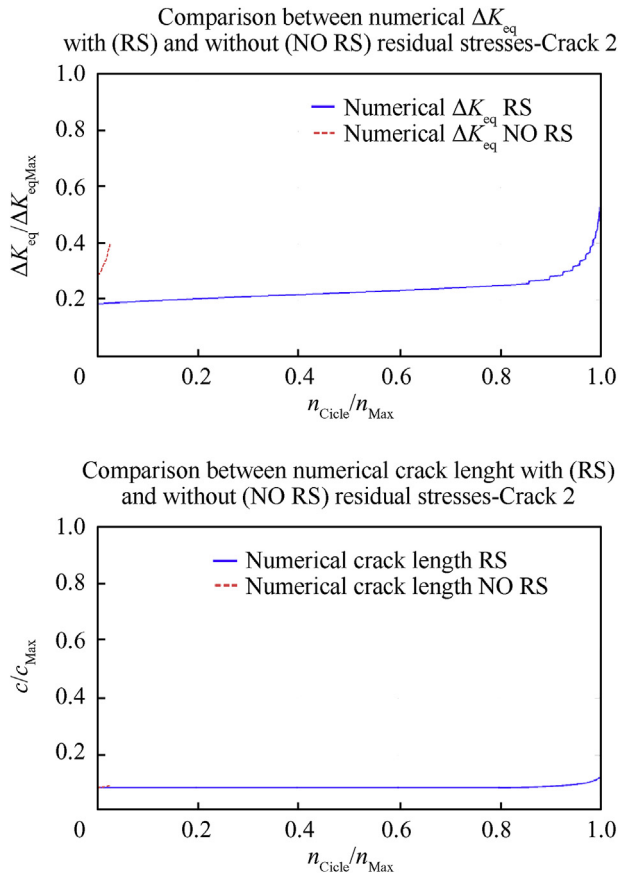
Fig. 9. Results of the analyses $C_{Max} = C_1$ − Crack 2. Comparison between results obtained with (RS) and without (NO RS) residual stresses. ΔK_{eq} vs n_{cycle} and crack propagation (c is the length of the crack) vs n_{cycle}.

Strain Gauges Rosettes (HBM RY9x type) were installed in three different critical locations of the shaft in order to record the variation of the stress state during the propagation of the crack, Fig. 10.

The position of each single rosette was:

- Rosette 1 was positioned close to the entry hole along the 45° line drawn along the axis of the holes at a distance of about 20 mm from the border of the hole (not inside the septum).
- Rosette 2 was positioned close to the exit hole along the 45° line drawn along the axis of the holes at a distance of about 20 mm from the border of the hole (not inside the septum).
- Rosette 3 was positioned on the other side of the shaft (180° from the damage) shifted along the generatrix, approximately at a distance from the nearest damage of 1 shaft diameter. This was a control sensor to verify the correct application of torque load.

Rosette 3 is therefore a control gauge that checks the accuracy of the torsional load whereas rosette 1 and 2 monitor the stress/strain field close to the damage and are thus affected by higher variability.

Rosettes were applied in order to monitor elastic variation due to the presence and propagation of the damage. Knowing the measured strains along the three directions the principal stresses were calculated. Experimental data and numerical results were compared in order to verify the accuracy of the numerical methodology. Considering the FE approach, a set of dedicated nodes was created and figures corresponding to the experimental ones were obtained. Considering the state of the plane stress, a dedicated routine was created to calculate the Maximum and Minimum principal stresses for each rosette and for each combination of crack lengths (for both the numerical and the experimental results). Due to the fact that rosette strain gauges were applied to the shaft after the impact, only the strain due to the load application was considered in the numerical model. Several numerical models were prepared for the various crack configurations and the models in close resemblance to available experimental data were considered. Considering, for example, the smallest torque load applied within the range step (C_1 Table 4), 20 different combinations of crack lengths (from L_{11}_L_{21} to L_{15}_L_{24}) were taken into account during the comparison, see Table 3. Rosette 2 consistently provided less data than the other two rosettes. This is due to the length of the crack 1 that reaches the location of the rosette 2 and doesn't permit the comparison of results during the propagation.

The comparisons of the results for each different load level (thus for the different tests) are shown in Figs. 11-15

The data are presented for each load case (see Table 4) and are reported as a function of the normalised number of cycles (see Fig. 15). The number of cycles were normalised over the maximum number of cycles achieved during the whole test campaign thus
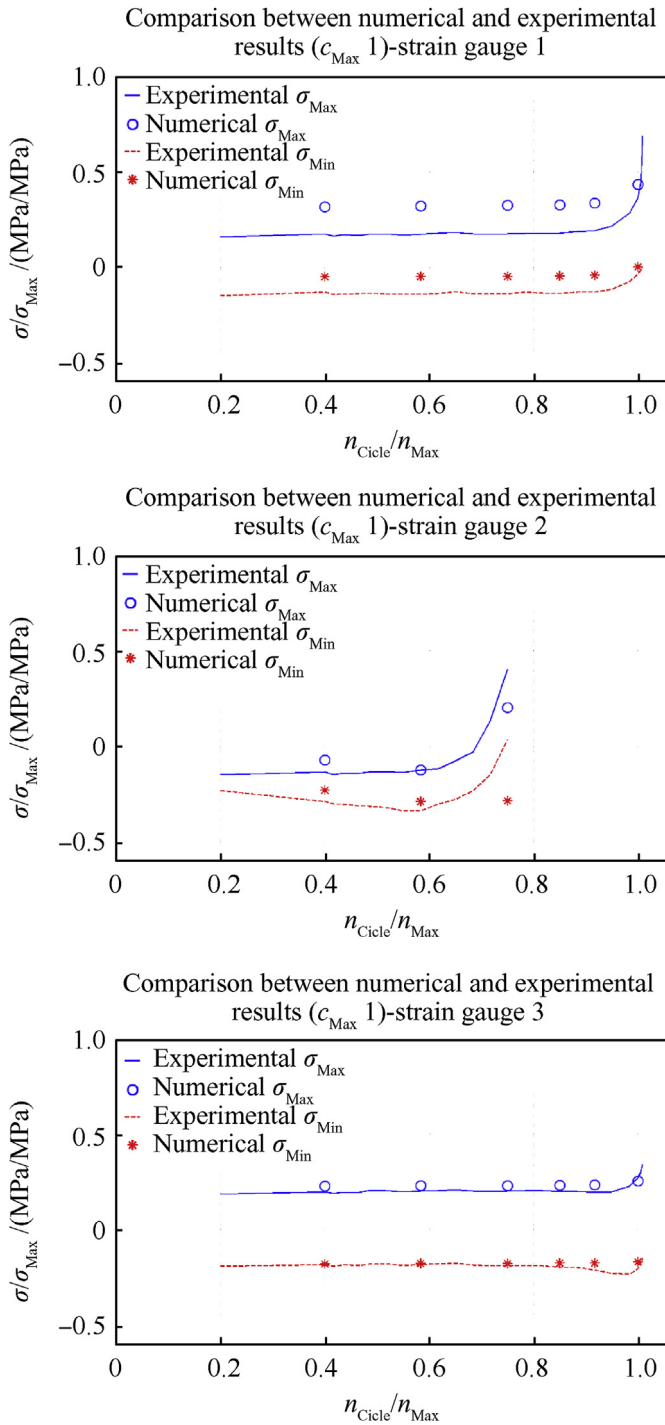

Fig. 10. Strain gauges rosette placement.

Fig. 11. Comparison between numerical and experimental results: Principal stress (Case C_1).

Fig. 12. Comparison between numerical and experimental results: Principal stress (Case C_2).

during test C_1. Numerical data (obtained at fixed steps of crack propagation) were associated to the cycles by means of experimental data (crack length vs. number of cycles). Some experimental data were neglected in Figs. 14 and 16 due to outliers caused by technical issues with the sensors. Figs. 12 and 13 show a divergent behaviour (between experimental and numerical data) at the very end of the test for strain gauge 3. In this case propagation of crack 2 starts only in the very last cycles. The simplified approach (the
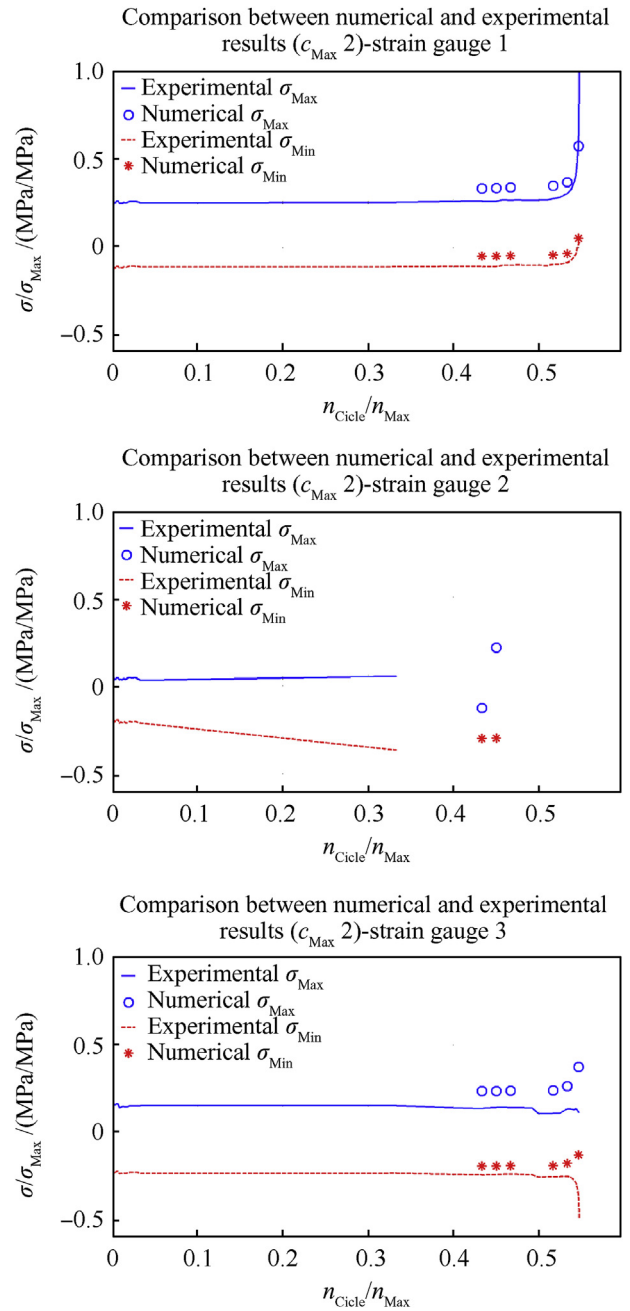
creation of models with discrete combinations of crack lengths) appears to be unable to correctly replicate the behaviour of the shaft in this condition. This is especially true in the zone of rosette 3 where the state of stress is generally due to pure torsion but varies drastically during the very last cycles and the failure may lead to a local instability.

However, the comparison clearly shows a similar behaviour of the numerical and experimental data. The figures further show how the numerical model slightly overestimates the stress in different cases. This behaviour is reflected also in the SIF calculation and in the final results, see Fig. 7, where the cycles to failure obtained by the numerical approach (with RS) are slightly lower with
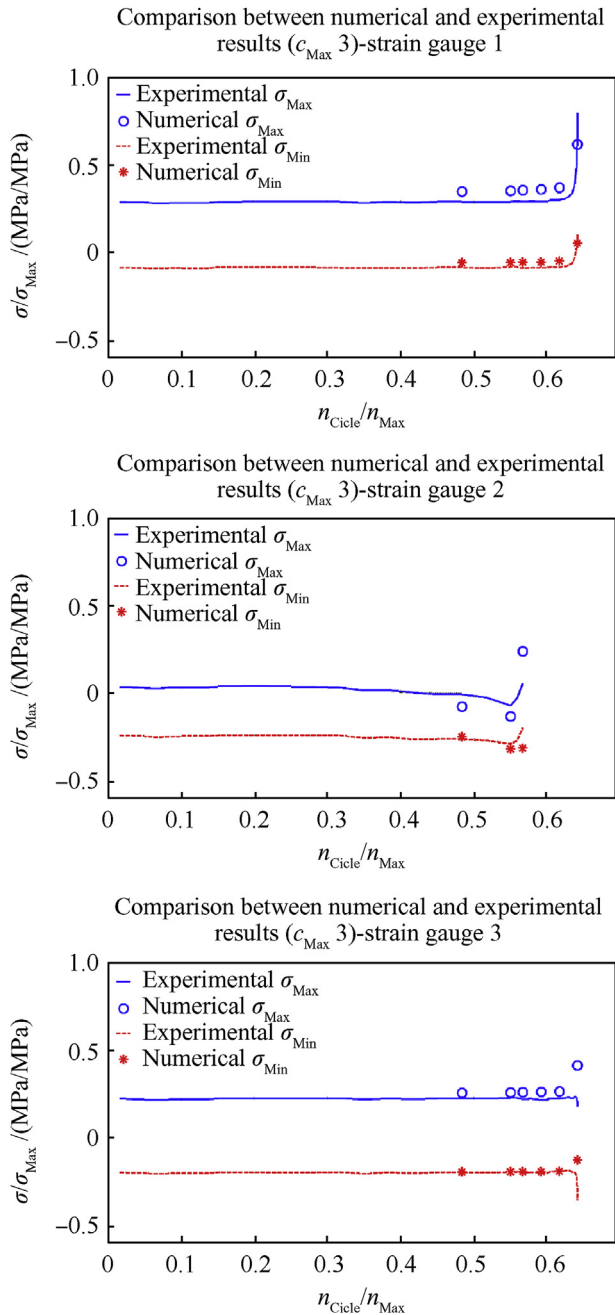
Fig. 13. Comparison between numerical and experimental results: Principal stress (Case C_3).

Fig. 14. Comparison between numerical and experimental results: Principal stress (Case C_4).

respect to the experimental data. As described above, the simulation of an actual spectrum load history was also considered by the numerical approach. The experimental tests show no propagation of the crack and the same results were obtained by the models (MATLAB routine). The strain data from the numerical model with no cracks was utilized to compare the experimental results in terms of strain field at different load levels. Fig. 16 reports the results for rosette 2 and rosette 3 (no experimental data are available for rosette 1). The numerical model of the shaft is clearly able to replicate the behaviour of the component under investigation with and without the presence of cracks.
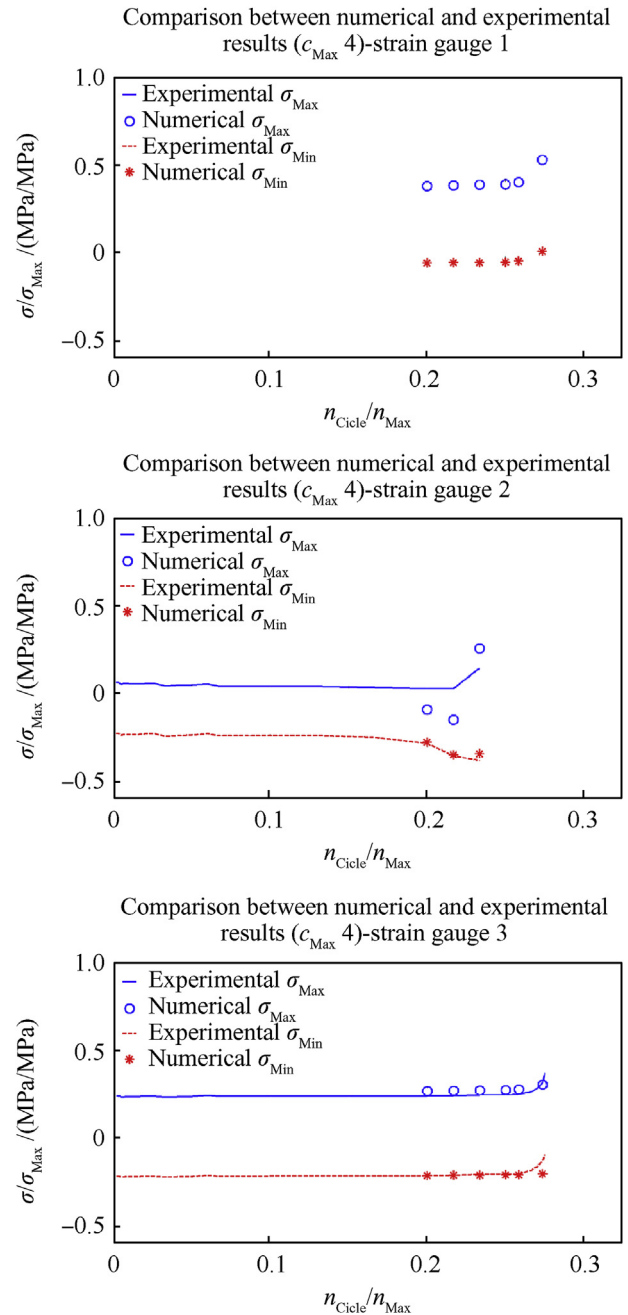
6. Conclusion

A numerical methodology for simulating fatigue cracks growth in an actual damaged component has been described and presented in this paper. The results from numerical simulations have been compared with experimental data showing good agreement. The proposed numerical methodology shows a very promising capability starting from the replication of the complex phenomena of ballistic impact and ending in an application of a delicate crack propagation analysis. It is important to remark that the accuracy and reliability of the data obtained from numerical modelling of the crack growth phase are strictly dependent on the results of the impact model. In this case, a methodology developed by the
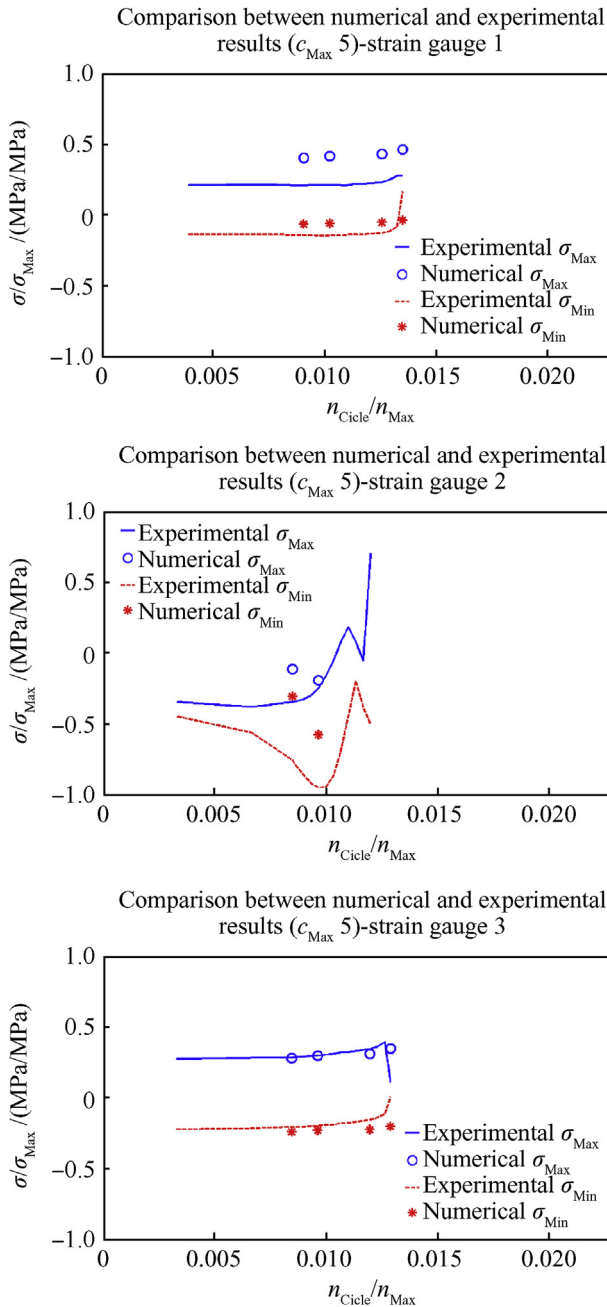
Comparison between numerical and experimental results (c_Max 5)-strain gauge 1

Comparison between numerical and experimental results (c_Max 5)-strain gauge 2

Comparison between numerical and experimental results (c_Max 5)-strain gauge 3

Fig. 15. Comparison between numerical and experimental results: Principal stress (Case C_5).

Comparison between numerical and experimental results-strain gauge 2

Comparison between numerical and experimental results-strain gauge 3

Fig. 16. Comparison between numerical and experimental results: Principal stress (Spectrum load).

costs. In this case, the peculiarity of the structure (a thin walled structure) and the choice (from experimental results) of a fixed propagation path reduced the complexity of the analyses. For thick components with a 3D propagation such an approach could be very time consuming. However, it is important to underline that the availability of such a modelling approach allows the testing (by virtual approach) of damaged items in a wide range of conditions, even in situations that could be unfeasible and/or very dangerous to verify by means of an experimental approach.

References

[1] Chan SLH, Tiong UH, Bil C, Clark G. Some factors influencing damage tolerance under helicopter spectra. Procedia Eng 2010;2:1497—504.
[2] Barlow KW, Chandra R. Fatigue crack propagation simulation in an aircraft engine fan blade attachment. Int J Fatig 2005;27:1661—8.
[3] FAR Part 29 Airworthiness Standards: Transport category rotorcraft.
[4] Lazzeri L, Mariani U. Application of Damage Tolerance principles to the design of helicopters. Int J Fatig 2009;31:1039—45.
[5] Tiong UH, Jones R. Damage tolerance analysis of a helicopter component. Int J Fatig 2009;31:1046—53.
[6] Newman Jr JC, Irving PE, Lin J, Le DD. Crack growth predictions in a complex helicopter component under spectrum loading". Fatig Fract Eng Mater Struct 2006;29:949—58.
[7] Maligno AR, Rajaratnam S, Lee SB, Williams EJ. A three-dimensional (3D) numerical study of fatigue crack growth using remeshing techniques. Eng Fract Mech 2010;77:94—111.
[8] Giglio M, Manes A, Viganò F. Numerical simulation of the slant fracture of a helicopter's rotor hub with ductile damage failure criteria. Fatig Fract Eng Mater Struct April 2012;35(Issue 4):317—27.
[9] Fossati M, Colombo D, Manes A, Giglio M. Numerical modelling of crack growth profiles in integral skin-stringer panels. Eng Fract Mech May 2011;78(7):1341—52.
[10] Manes A, Lumassi D, Giudici L, Giglio M. An experimental-numerical investigation on aluminium tubes subjected to ballistic impact with soft core 7.62

authors in previous research activities has been exploited in order to obtain a realistic simulation of the impact. The damage morphology as well as the residual stresses are key features have been reproduced in order to obtain a reliable "test bed" for the subsequent fatigue/crack propagation analyses. The introduction of the residual stress state (caused by the impact of the projectile) within the numerical model during the identification of the K factors, is a decisive feature. Indeed, the comparison of the results clearly shows how the models with residual stresses can accurately represent the damage tolerant characteristic of the component subjected, after a ballistic impact, to torsion fatigue load cycles. It is worth mentioning that the exploitation of such an approach in real-world cases is still very complex due to the high computational
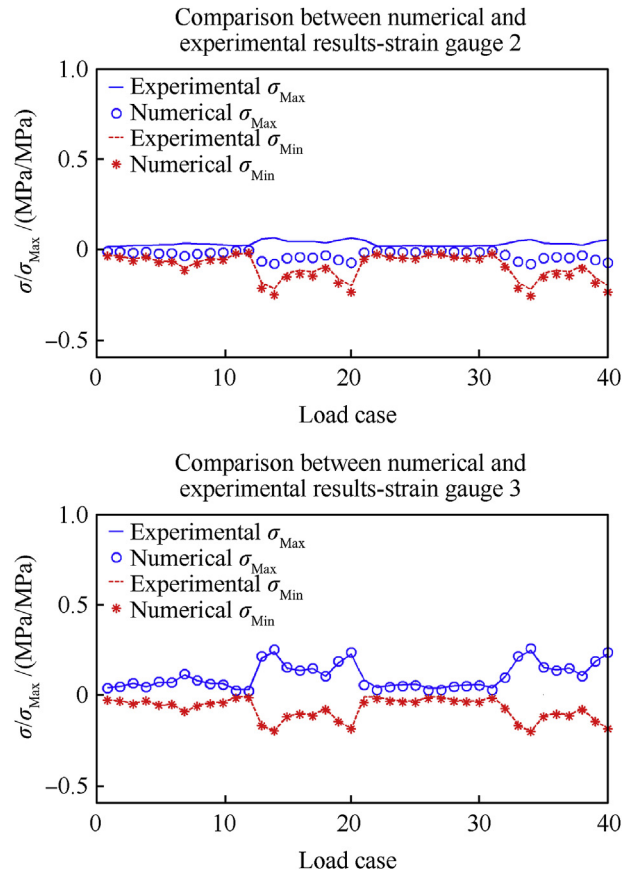
ball projectiles. Thin-Walled Struct 2013;73:68—80.

[11] Melenk J, Babuska I. The partition of unity finite element method: basic theory and applications. Comput Methods Appl Mech Eng 1996;139:289—314.

[12] Belytschko T, Black T. Elastic crack growth in finite elements with minimal remeshing. Int J Numer Methods Eng 1999;45:601—20.

[13] Moes N, Dolbow J, Belytschko T. A finite element method for crack growth without remeshing. Int J Numer Methods Eng 1999;46:131—50.

[14] Feulvarch E, Fontaine M b, Bergheau JM. XFEM investigation of a crack path in residual stresses resulting from quenching. Finite Elem Anal Des 2013;75: 62—70.

[15] Singh IV, Mishra BK, Bhattacharya S, Patil RU. The numerical simulation of fatigue crack growth using extended finite element method. Int J Fatig 2012;36:109—19.

[16] Fengmei X, Fuguo L, Jiang L, Min H, Zhanwei Y, Ruiting W. Numerical modeling crack propagation of sheet metal forming based on stress state parameters using XFEM method. Comput Mater Sci 2013;69:311—26.

[17] Gilioli A, Manes A, Giglio M, Wierzbicki T. Predicting ballistic impact failure of aluminium 6061-T6 with the rate-independent Bao-Wierzbicki fracture model. Int J Impact Eng February 2015;76:207—20.

[18] NASGRO 4.11, reference manual. NASA Johnson Space Center; 2004.

[19] Manes A, Serpellini F, Pagani M, Saponara M, Giglio M. Perforation and penetration of aluminium target plates by armour piercing bullets. Int J Impact Eng 2014;69:39—54.

[20] Zukas JA. High velocity impact dynamics. New York USA: Wiley; 1990.

[21] Colombo D, Giglio M, Manes A. 3D fatigue crack propagation analysis of a helicopter component. Int J Mater Prod Technol 2007;30(Nos. 1/2/3).